

Electronic Interactions and Stability Issues at the Copper-Graphene Interface in Air and in Alkaline Solution under Electrochemical Control

Salma Khatun^{1, ‡}, Miguel A. Andrés^{1, ‡}, Sidney R. Cohen², Ifat Kaplan-Ashiri²,
Olga Brontvein², Irit Rosenhek-Goldian², Robert S. Weatherup³, Baran Eren^{1,*}

¹Department of Chemical and Biological Physics, ²Chemical Research Support, Weizmann
Institute of Science, 234 Herzl Street, 76100 Rehovot, Israel,

³Department of Materials, University of Oxford, Parks Road, Oxford, Oxfordshire, OX1 3PH,
United Kingdom

[‡] Equal contribution

Corresponding Author

*Baran Eren, E-mail: baran.eren@weizmann.ac.il, Phone number: +972 8-934-3708.

ABSTRACT: A micro-electrochemical cell is sealed with a polymer-free single-layer graphene (SLG) membrane to monitor the stability of Cu nanoparticles (NPs) attached to SLG, as well as the interfacial electronic interactions between Cu NPs and SLG both in air and in a mildly alkaline aqueous solution under electrochemical control. A combination of techniques, including in-situ Kelvin probe force microscopy (KPFM) and ex-situ electron microscopy, are applied. When Cu NPs are metallic at cathodic potentials, there is a relatively bias-independent offset in the SLG work function due to charge transfer at the Cu-SLG contact. When Cu NPs are oxidized at anodic potentials, on the other hand, the work function of SLG also depends on the applied bias in a quasi-linear fashion due to electrochemical gating, in addition to charge transfer at the CuO_x -SLG contact. Furthermore, Cu NPs were found to oxidize and detach from SLG when kept under anodic potentials for a few hours, whereas they remain adhered to SLG at cathodic potentials. This is attributed to water intercalation at the CuO-SLG interface associated with the enhanced hydrophilicity of positively polarized graphene, as supported by the absence of Cu detachment following oxidation by galvanic corrosion in air.

Keywords: In-situ KPFM, copper nanoparticles, redox, graphene, interfacial stability.

1. INTRODUCTION

Electrochemistry is one of the oldest fields in the natural sciences and it still plays a central role in contemporary energy storage and chemical conversion technologies [1-2]. Despite its rich history, current descriptions of electrode-electrolyte interfaces are to a large extent limited to continuum electrical double layer (EDL) models, ensemble experiments (e.g., cyclic voltammetry (CV), impedance spectroscopy, etc.), and *ex-situ* characterization techniques (e.g., electron microscopy) for determining chemical composition, chemical state, and morphology of the electrodes and EDL after the reaction has taken place. Probing the electrified interface between an electrode and a liquid solution during a reaction is a daunting task. Over the past few decades, there have been significant advances in various spectroscopic and microscopic methods that can probe these interfaces under operating conditions; each one of these methods marked by both advantages and drawbacks, as summarized in ref. [3]. Information obtained from such *in-situ / operando* spectroscopy techniques has greatly improved our present understanding of the solid / liquid interfaces. Apart from the spectroscopic techniques, electrochemical scanning tunneling microscopy (EC-STM) stands out as the most commonly used technique for characterization of electrode-electrolyte interfaces with high resolution [4-5]. Another scanning probe technique that could be of substantial importance for electrochemical systems is Kelvin probe force microscopy (KPFM), which is a variant of atomic force microscopy (AFM) that is extensively used to map work function (WF) variations of materials both in ambient or vacuum conditions [6]. It, however, has technical limitations; most importantly, it cannot be used in polar liquids unless employing open-loop KPFM [7-8], or by more specialized adaptations that are not widely available [9].

Capping a micron-sized reactor-cell with a graphene-membrane is an alternative approach to

traditional means of conducting spectroscopic and microscopic experiments. Reactor-cells utilizing the graphene-membrane approach have already been shown to be feasible for electron microscopy and x-ray spectroscopy techniques [10-17]. In our previous work, we applied this approach for KPFM and Raman spectroscopy measurements, presenting the WF changes in single layer graphene (SLG) suspended on an alkaline aqueous solution under electrochemical reaction conditions [18]. Since KPFM is a direct electrostatic measurement, it is ideal for probing the electronic interactions between SLG and other materials attached to it. We show here that the graphene-membrane approach for electrochemical measurements can be extended to functional materials such as transition metal / transition metal oxide nanoparticles (NPs).

In this study, the interface between Cu NPs and SLG serves as the model system. Cu surfaces are well-established catalysts for electrochemical reduction of CO₂ into valuable products [19-20], while utilizing carbon-based materials as a supporting substrate [21-23]. However, prior to establishing the catalytic activity and surface chemistry of Cu NPs under electrochemical CO₂ reduction conditions, their interfacial stability during electrochemical oxidation and reduction conditions should be addressed. The most important concerns are the electronic decoupling and physical detachment of Cu NPs from the SLG support, and dissolution of the Cu NPs during either oxidation or reduction. The issue of electronic decoupling at the graphene-Cu interface was mainly investigated in the literature on polycrystalline Cu supports in the context of intercalation of oxygen-containing species (e.g., oxygen, water vapor) from ambient air. Studies performed with x-ray photoelectron spectroscopy (XPS) and Raman spectroscopy showed that electronic decoupling of graphene from the substrate accompanies the intercalation of such species and the formation of an oxide layer on the Cu surface [24-25]. Interestingly, annealing such samples in vacuum reverses the electronic decoupling as the oxide

is reduced [24]. A more severe phenomenon that takes place at the graphene-Cu interface is corrosion: Although graphene provides an effective protection of underlying Cu substrates from short-term oxidation [26-27], long-term exposure to air causes galvanic corrosion [27-30]. The galvanic corrosion on polycrystalline Cu depends on the crystal orientation, in such a way that grains with lower WF (due to higher atomic corrugation), specifically those with a WF lower than that of graphene, are subject to corrosion [30]. Furthermore, whilst galvanic corrosion takes months in air, polycrystalline grains were corroded in a couple of days inside deionized water [30]. Finally, dissolution of Cu NPs could be a problem in acidic or alkaline solutions even at open circuit potential (OCP).

In this work, we evaporated Cu on SLG to form NPs with random shape and size. Initially, we investigated the stability in ambient conditions, observing oxidation over the course of a month, similar to the oxidation of corrugated grains in previous studies [27-30]. We did not observe any material loss. Using *in-situ* KPFM measurements combined with *ex-situ* electron microscopy analysis, we further investigated the changing oxidation state of Cu in an alkaline medium, as well as its electronic coupling to SLG and interfacial stability under various constant-potential reaction conditions. Whilst Cu NPs undergo oxidation and reduction as expected, we observed loss of material due to detachment of NPs from SLG at anodic potentials. We associate this behavior with electro-wetting of graphene that enhances water intercalation at the interface between SLG and oxidized Cu. These results raise questions about the use of carbon-based materials as supports for materials for Cu, especially in oxidized form at anodic potentials. We believe that this work serves as a benchmark for further studies in the characterization of electrochemical interfaces on transition metal / transition metal oxide NPs in aqueous solutions.

2. EXPERIMENTAL SECTION

2.1 Sample Preparation

Graphene-membranes were prepared using the approach described in ref. [17-18]. In brief, chemical vapor deposition (CVD)-grown single-layer graphene (SLG) on polycrystalline Cu foil was transferred onto Au(30 nm)-coated SiN_x grids (with a 200 nm thick window in the center, Ted Pella Inc, USA) with an array of perforations (450×450 μm² array of ø~500 - 600 nm). Prior to transferring SLG, Cu foil was etched in a Na₂S₂O₈ solution followed by diluting the etchant solution with a few liters of deionized water. SLG suspended on deionized water was then fished out with an Au-coated SiN_x grid. Complete details of the transfer can be found in ref. [18]. The Au coating (deposited by e-beam evaporation) ensures electrical continuity over large-areas even in the presence of localized tears in the SLG. A distinguishing and crucial factor in our preparation method is the transfer of graphene without the use of a support polymer, in order to avoid polymer residues that can influence charge-carrier doping, and potentially cause additional side reactions. Cu was evaporated on the backside of the sample with a nominal thickness of 1 nm, resulting in the formation of Cu NPs, as shown in the scanning electron microscopy (SEM) image in Figure 1a. The samples were then annealed to 300 °C in ultra-high vacuum (UHV) for 4 h in order to desorb water and hydrocarbon contaminants, which also resulted in sintering of the Cu NPs, as shown in Figure 1b. These sintered Cu NP clusters were used in the rest of the experiments in this work. The presence of Cu NPs changes the topography and phase contrast in intermittent-contact mode AFM images. Figures 1c and 1d show the topography and phase images of suspended SLG in the absence of NPs, which both exhibit a rather uniform profile across the membrane. In the presence of Cu NPs, the topography takes on corrugation in the

form of thin web-like features with a height difference of around half a nanometer (Figure 1e). This pattern can be better observed in the corresponding phase image, since the phase contrast depends on viscoelastic properties of the surface, which is affected by the presence of Cu NPs behind the membrane (Figure 1f). We performed XPS measurements after annealing (without breaking the vacuum) to confirm the relative cleanliness of the sample. No elements other than Cu, C, O, and Au were detected (Figure S1). Oxygen species likely relate to the functionalization of certain defect sites of CVD-grown graphene. Hydrogen, which is also expected to functionalize defect sites, cannot typically be detected with lab-source XPS.

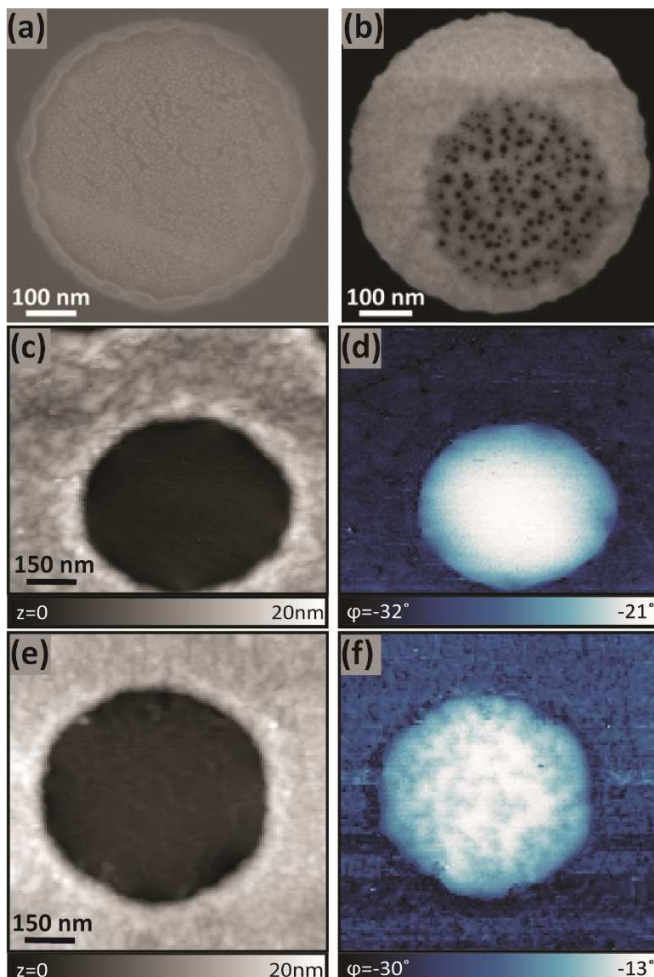


Figure 1. SEM images of a suspended-SLG region with Cu NPs under the SLG; (a) after evaporation of 1 nm Cu and (b) after annealing in UHV at 300 °C for 4 h. Whilst the NPs are evenly distributed after deposition, they sinter into a cluster after annealing. An electron energy of 5 keV and scanning transmission electron microscopy (STEM) detectors were used for both images. Whilst (a) is a high angle annular dark-field image, (b) is a bright-field image. AFM topography (c,e) and phase (d,f) images of a circular suspended-SLG region; (c-d) bare suspended-SLG, (e-f) with Cu NPs underneath the SLG similar to (b). Our samples consist of thousands of such circular suspended-SLG regions, covering a total area of 450×450 μm². All image acquisition started ~30 min after the samples were removed from the UHV chamber.

2.2 Reactor-cell Design

Electrochemical experiments were performed using a custom micro-reactor in a two-electrode configuration [18], as shown in Figure 2a, connected to a potentiostat (SP-200, BioLogic). A ∅1 mm Pt wire served as both the counter electrode (CE) and the pseudo-reference electrode, and SLG/CuNPs served as the working electrode (WE). The electrolyte is enclosed in a polyether ether ketone (PEEK) housing, and sealed with the SiN_x grid (∅3 mm) sandwiched between a perfluoroelastomer O-ring and stainless steel lid, which has a ∅2 mm aperture. We used a mildly alkaline aqueous NaOH solution (10⁻⁴ M) as electrolyte. To characterize the electrochemical behavior in this cell, we performed CV measurements with a scan-rate of 0.02 V/sec (Figure 2b). As a two-electrode system is used instead of three electrodes due to geometric restrictions, we cannot compare the exact positions of the oxidation and reduction peaks of Cu with those published in the literature. Nevertheless, they can be definitively assigned on the CV curve as shown in Figure 2b. As-prepared Cu is initially oxidized due to ~30 min storage in air, and it goes through a two-step reduction process during the cathodic scans: $\text{CuO} + \frac{1}{2}\text{H}_2\text{O} + e^- \rightarrow$

$\frac{1}{2}\text{Cu}_2\text{O} + \text{OH}^-$ and $\frac{1}{2}\text{Cu}_2\text{O} + \text{e}^- + \frac{1}{2}\text{H}_2\text{O} \rightarrow \text{Cu} + \text{OH}^-$, while the reverse oxidation process takes place during the anodic scans [31-33]. Importantly, the Cu(II) oxidation state obtained at anodic potentials is likely a mixture of CuO and Cu(OH)₂ [34-35]. The assignment of the peaks to Cu electrochemical processes is confirmed by comparing CV data obtained with SLG/CuNPs as the WE to those using bare SLG as the WE for which no such redox peaks are observed in the same bias range (Figure S2). Moreover, the current is three orders of magnitude lower for bare SLG compared to SLG/CuNPs (pA vs. nA) (Figures S2 and 2b). It should be noted that the surface area of the Cu is three orders of magnitude lower than the surface area of Pt in our configuration. This corresponds to a current density of the redox peaks in the range of mA/cm₂ for Cu and $\mu\text{A}/\text{cm}_2$ for Pt. Although a 3-electrode configuration would be preferable this is challenging within the geometric constraints of the cell. However additional 3-electrode measurements (Figure S3) using performed using electrodes with similar surface area ratios, and a Ag/AgCl (3M KCl) reference electrode (RE), confirm that the current density passing through the CE is low enough that positions of the main Cu features with respect to the CE remain within 0.1 V of those measured with respect to the RE. The stability of the peak positions in the voltammogram of Figure 2b confirms the stability of peak positions over repeated cycles further confirming the suitability of the micro-reactor for electrochemical studies.

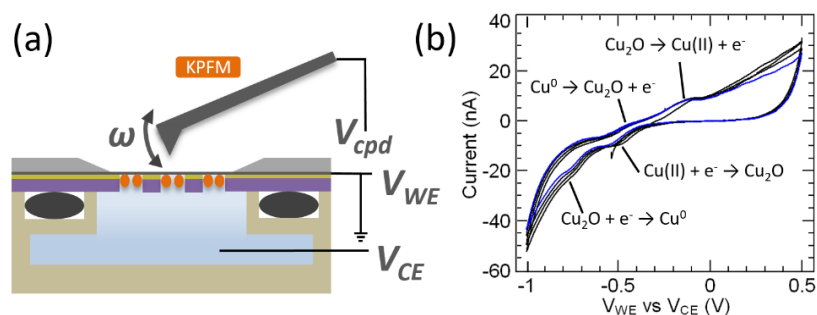


Figure 2. (a) Schematic of the electrochemical micro-reactor for *in-situ* KPFM measurements. ω indicates the oscillating cantilever. Orange circles represent the Cu NPs underneath the SLG layer. V_{WE} and V_{CE} are potentials on the working and counter electrodes, which are connected to a potentiostat. V_{cpd} is the measured contact potential difference between AFM tip and surface. (b) CV measurements performed with this cell. Blue curve shows the last cycle out of 5 cycles. Oxidation and reduction peaks in the CV are indicated on the graph, with proposed reactions from the literature [31-35]. Collection of CV data started ~30 min after the sample was removed from a UHV chamber.

2.3 Characterization Methods

In-situ KPFM experiments were performed with an NTEGRA Smena AFM (NT-MDT, Russia) using amplitude modulation (AM). We employed a two-pass scanning mode: topography and phase signals were recorded in the first scan, followed by a 10-14 nm lift of the tip for recording the Kelvin signal in the second scan. A setpoint oscillation amplitude (A_{sp}) of around 80-90% of the free oscillation amplitude ($A_0 = 50-75$ nm) was used in order to get distinct phase contrast. The Kelvin controller cancels electrostatic forces by adjusting the tip bias voltage (V_{dc}) to return a signal equal to the contact potential difference (CPD) between the tip and the sample. The regions between the circular suspended-SLG regions, where SLG rests directly on the Au-coated grid are not exposed to the solution and hence are not expected to be affected by changes in applied electrochemical potential. Since the KPFM signal represents the CPD between tip and surface, variation of the WF of suspended-SLG regions is monitored with reference to those supported regions, and is referred to as CPD contrast (ΔCPD) throughout the rest of the manuscript. A brighter CPD contrast corresponds to a lower local WF.

SEM imaging was performed using a Zeiss GeminiSEM 500 high-resolution microscope. The images were acquired at 5 kV landing voltage with the InLens detector (secondary electron detection) and the STEM detector (transmitted electron detection) in bright-field and high angle annular dark-field modes. Transmission electron microscopy (TEM) measurements were performed with a Talos F200X microscope equipped with Super-X energy-dispersive X-ray spectroscopy (EDS) detector. The images were acquired at an electron energy of 200 keV.

3. RESULTS AND DISCUSSION

3.1 Interfacial stability issues

In air

We start our analysis by discussing the oxidation state of the Cu NPs in ambient air conditions, as the oxidation state could both influence the charge-transfer between the SLG and NPs and enhance/enable intercalation of water at the Cu-SLG interface. XPS of the Cu 2p region (Figure S1) suggests that after annealing in UHV the Cu NPs are either in the form of Cu⁰, Cu₂O, or a mixture of these two oxidation states, which is difficult to distinguish as the main features have similar binding energies [17,36]. The intensity in the O 1s and Cu LMM regions is not high enough in this instance to differentiate between these two oxidation states. Reduction of CuO into Cu₂O upon annealing in UHV has been reported both in our previous work and by others [17,37-38]. The samples for KPFM measurements were exposed to air for around 30 minutes after the UHV-annealing, which likely leads to oxidation of the Cu NPs. In earlier studies on Cu thin films, it was found that CuO builds up only on the uppermost layer (around 1.3 nm) directly exposed to air for 2 days, with Cu₂O (around 2 nm) forming below this. [39]. In the current study, the side of the Cu NP clusters attached to SLG may have less direct exposure to air,

however diffusion of oxygen species is still expected through atomic-scale defects in the SLG [30].

In order to monitor the corrosion process taking place in air, we performed EDS analysis on the Cu NPs after 2 days and 30 days of exposure to air. Figure 3 shows the bright-field STEM images and the EDS maps of Cu (yellow) and oxygen (red). On larger NPs ($\varnothing > 10$ nm), the oxygen signal is higher at the NP edges compared to their cores after 2 days of storage, whereas a more homogenous distribution is observed after 30 days of storage. To roughly quantify this difference, we performed a statistical analysis on the Cu:O ratio of 20 different NPs in both conditions. After two days of storage in air, the Cu:O ratio is 1.4 ± 0.4 for the shell (we define the shell as the outer 2.5 nm thick layer) and 3.2 ± 0.7 for the core of the NPs. For the set of NPs stored 30 days in air, we obtained a Cu:O ratio of 0.7 ± 0.1 for the shell and 1.2 ± 0.2 for the core. These ratios are underestimations for the core of the particles, because it is a transmission measurement that also includes shell regions with higher amount of O. They are also underestimations for the shell of the particle, because the surface of the particles are likely covered with hydroxyls due to storage in air. Moreover, SLG defects are functionalized with oxygen (Figure S1), which results in additional underestimation of the Cu:O ratio both for the core and the shell of the NPs. Nevertheless, we can conclude that after 2 days the shell is a mixture of Cu_2O and CuO and the core is a mixture of Cu_2O and Cu . After 30 days, the core is a mixture of Cu_2O and CuO and the shell is largely CuO . In terms of morphology and particle size distribution, there is no noticeable difference in the bright-field STEM images between the top and bottom set of images in Figure 3, suggesting that corrosion in air did not result in any stability issues that lead to significant material loss or agglomeration.

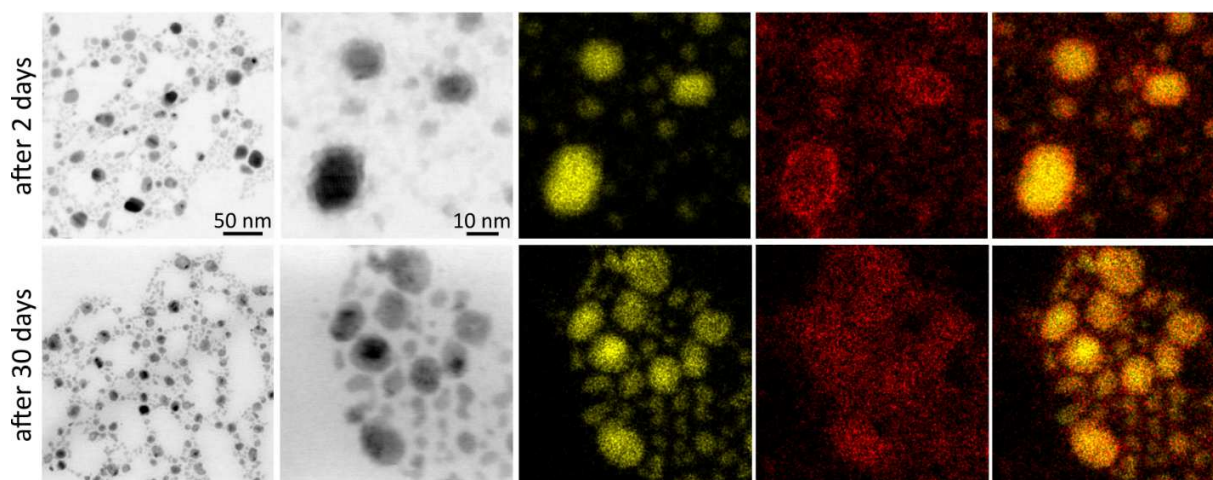


Figure 3. Bright-field STEM images and EDS analysis on one of the prepared samples after two days (top set of images) and thirty days (bottom set of images) of exposure to air. In EDS maps, Cu is yellow and oxygen is red. The scales in the lower row are the same as in the upper row.

In alkaline solution under electrochemical control

Oxidation and corrosion of Cu NPs in an electrolytic cell will differ from that of a galvanic cell, as Faradaic reactions are not spontaneous but driven by an applied potential. Harsher conditions are therefore accessible that could lead to interfacial stability issues.

Ex-situ SEM images provide evidence for changes in the morphology of Cu NP clusters associated with material loss in the NaOH electrolyte at constant-potential. Figure 4a shows a SEM image of the Cu NP clusters acquired after ~10 hours of KPFM measurements at various electrochemical potentials (shown later in Figure 6c). Compared to the initial morphology (Figure 1b), the coverage of Cu NPs on SLG is lower after the experiments (Figure 4a). This is also the case for Cu NPs that had a higher initial coverage due to more Cu deposition (i.e., larger as a sintered cluster, Figure 4b). The Cu NP clusters also appear porous in both Figures 4a and 4b. In Figure 4b, some of Cu NP clusters appear unchanged (marked with yellow arrows), which

suggests that they either had no contact with the electrolyte solution during the experiments or they were electrically isolated from the SLG already before the experiments. The former is considered more likely, as: (i) we do not observe CPD variations between the different circular regions in dry conditions for this sample, suggesting similar interfacial charge exchange between Cu and SLG for each region (explained in detail in Section 3.2). (ii) some of the circular regions do not show significant changes in CPD with potential under electrochemical control. After the CV experiments shown in Figure 2b, which require much less time, we did not observe such major changes in the morphology of the Cu NP clusters (Figure S4). Lack of material loss during CV explains the minimal difference in the intensity of the redox peaks in Figure 2b after the first cycle. We can thus conclude that Cu NPs are stable on SLG for a short period at high $|V_{WE}$ vs $V_{CE}|$, but not for longer exposure. In the SEM images in Figure 4b, we also observe rupturing of SLG (marked with blue arrows), which is not typically observed for bare SLG [18].

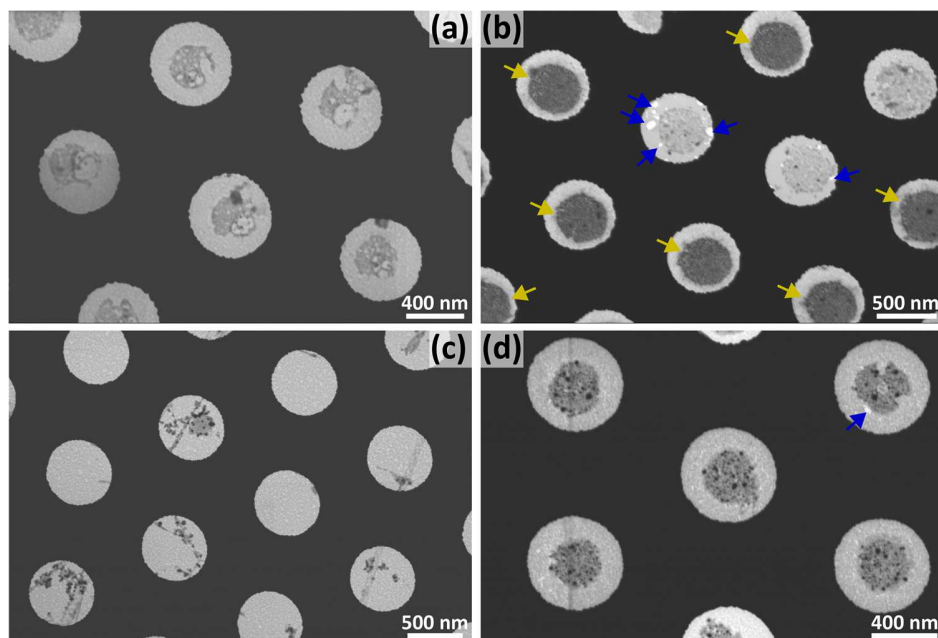


Figure 4. *Ex-situ* SEM images collected with a bright-field STEM detector. (a and b) Images after experiments with various constant-potentials ranging from -1 V to 1 V; (a) the sample used in main KPFM experiments shown in Figure S5, (b) the sample used in test KPFM experiments shown in Figure S6. Note that not all the circular regions fully respond to the applied potential for (b) during KPFM imaging. (c) After 3 hours at 1 V vs V_{CE} , and (d) after 3 hours at -1 V vs V_{CE} . Yellow arrows in (b) indicate Cu NP clusters that were not affected due to lack of contact with the liquid. Blue arrows in (b) show ruptured areas in SLG.

In order to rationalize the cause of material loss during our experiments, we performed test experiments, in which two different samples were kept at a potential of 1 V and -1 V (vs V_{CE}) for 3 hours after one cleaning cycle, shown in Figures 4c and 4d. These images clearly indicate that the changes in the morphology of Cu NP clusters associated with material loss occurs under oxidizing, but not reducing conditions.

The loss of Cu can be rationalized by two alternative phenomena: First, it could be due to the formation and dissolution of $Cu(OH)_2^-$ at around 0 V vs the standard hydrogen electrode (SHE), as suggested by the Pourbaix diagrams at room temperature in ref. [41]. However, this is expected to play only a minor role, as solid CuO or $Cu(OH)_2$ formation is preferred over the formation of $Cu(OH)_2^-$ ions at anodic potentials. Secondly, formation of an oxide at the SLG-Cu interface may not just relate to electronic decoupling of Cu from SLG, but also detachment associated with intercalation of water at the interface. In order to confirm that detachment of NPs is indeed the reason behind material loss, we prepared another sample with 1 nm Cu covering an

Au surface and kept it at 1 V (vs V_{CE}) for 3 hours. Unlike Cu NPs supported on SLG, Cu NPs on Au remained intact, as confirmed with EDS analysis.

These results suggest that Cu NPs supported on SLG detach from SLG at anodic potentials, under which full oxidation occurs. At such potentials, graphene can become hydrophilic for two reasons: it is oxidized to form graphene oxide (which we confirm by Raman spectroscopy) and it is polarized due to electronic doping [18]. We therefore rationalize the detachment of NPs directly due to the intercalation of water at the CuO-SLG interface, enabled by the strong electro-wetting of graphene. No detachment of NPs takes place in air at the same CuO-SLG interface (in air the Cu surface is oxidized due to galvanic corrosion as discussed above), as SLG is hydrophobic in air [42]. The fact that no loss of Cu is observed at negative potentials can be explained by a lesser degree of hydrophilicity and electro-wetting compared to positive potentials: Graphene oxide is reduced to 'reduced graphene oxide' at such potentials [18], which is less hydrophilic than graphene oxide. Non-functionalized sites of graphene are also less hydrophilic under negative polarization compared to positive polarization [18]. Therefore, water intercalation is less likely to take place at cathodic potentials. In addition, metallic Cu couples more strongly to graphene than oxidized Cu [24-25], which also makes water intercalation less likely at cathodic potentials.

We note the observed detachment at positive potentials does not reflect on the validity of applying this approach to studies on Cu-catalyzed CO₂ reduction, which takes place at cathodic potentials [43]. However, at negative potentials localized tearing of the SLG is observed, as seen in Figure 4d for a sample held at -1 V (vs V_{CE}). This could be due to the mechanical stress caused by the accumulation of evolved hydrogen gas (Figure S7), but interestingly no such

rupture is seen for a sample held at 1 V (vs V_{CE}) indicating SLG oxidation or accumulation of oxygen gas do not cause rupture (see Figure 4c).

TEM-EDS analysis was performed on most of the samples that were treated under various electrochemical conditions in this work. Traces of Pt, which have been reported as a potential problem in previous work [44-45], were not observed on any of our WEs.

3.2 Electronic Interaction between SLG and Cu NPs

In air

Figure 5 shows KPFM measurements performed on a test sample, after roughly 30 min exposure to air. During the preparation of this sample, half of the sample was shadowed during Cu deposition whereas the other half remained exposed. As the reference is the same SLG/Au in both cases, we can directly compare the CPD of the suspended regions with and without Cu deposition. On the unexposed half of the sample, the CPD is brighter (higher) for the suspended regions with $\Delta CPD \approx 0-20$ mV. This can be rationalized by noting that Au is a noble metal with a filled outer d -shell, and thus does not strongly hybridize with graphene and disrupt its linear π -band dispersion but instead dopes it through charge transfer [46]. Given the higher WF of Au, electrons are removed from the SLG shifting its Fermi energy (E_F) towards the valence band and resulting in a higher WF relative to suspended SLG.

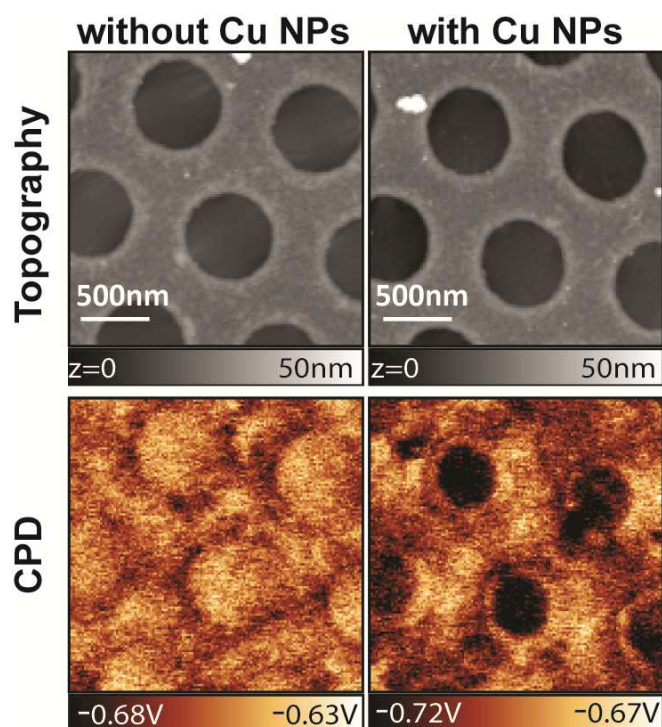


Figure 5. Topography and CPD images of the samples. The presence of Cu NPs (their surface is in the Cu_xO ($1 \leq x \leq 2$) oxidation state) behind the SLG inverts the CPD contrast. Measurements were performed with the same tip and the same grid, with images on the left (no Cu) and right (with Cu) columns representing regions shadowed and exposed during the evaporation, respectively. The sample was exposed to air for ~30 min prior to imaging.

On the half of the sample exposed to Cu, the presence of the Cu NP clusters behind the SLG reduces the CPD below that of the SLG/Au regions, i.e., SLG/CuNPs regions show a $\Delta\text{CPD} \approx -30$ mV. Thus, overall Cu deposition results in a decrease of the CPD of SLG suspended in air by 30-50 mV. This implies that the Cu NPs cause the E_F to move further towards the valence band resulting in a higher WF than SLG/Au. This is contrary to what is expected for metallic NPs since Cu was reported to introduce electron doping in graphene [46-48]. Since metallic NPs have

even lower WF than the equivalent semi-infinite surfaces, they should induce even higher levels of electron doping [47,49]. Exposure to air directly or at the SLG interface through defects thus seems to oxidize the NP surfaces. This is in agreement with a report that the WF of SLG is elevated by contacting to oxidized Cu [47]. Assuming Cu_2O formation at the interface between Cu and SLG, the observed shift in the E_F can be rationalized based on electron transfer from SLG to Cu_2O , in line with its p-type semiconducting nature [50-51]. CuO is also a p-type semiconducting oxide [52], but as mentioned earlier, its formation could electrically decouple the NPs from SLG, i.e., the shift in SLG WF should be smaller. We can thus consider the surface of the Cu NPs as Cu_xO ($1 \leq x \leq 2$) prior to redox reactions, where electrical interaction with the SLG results in hole doping.

It is also instructive to consider the physical phenomena that are probed by KPFM measurements. In the case of a metal, KPFM measures the true WF of the material, that is, the chemical potential of an electron in the bulk increased by the surface dipole layer. Once graphene weakly adsorbs on a metal surface, it modifies the surface dipole layer due to charge exchange at the interface, and thereby modifies the metal WF. The surface dipole layer of the metal altered by the charge transfer can also be considered as graphene that is doped by an underlying metal through charge transfer. Both yield the same WF of the graphene/metal system as measured above the surface, for instance by KPFM or other techniques. The situation is somewhat altered for graphene covering a dielectric and/or semiconductor substrate. Although the graphene can be doped by charge transfer from the underlying substrate, the KPFM signal, which is dependent on the capacitance between tip and surface, detects the overall capacitance extending several nm below the surface. [53-54]. In the present case, the capacitance of the NPs contribute to the signal in the form $[C_{\text{tip-surface}} * C_{\text{NP}}] / [C_{\text{tip-surface}} + C_{\text{NP}}]$. Since both the average tip-sample distance

is larger than the thickness of the NPs, and the permittivity of copper oxides is much higher than that of air, C_{NP} is relatively large and the expression becomes almost equal to $C_{tip-surface}$. Thus, any contribution due to capacitance of the NPs can be ignored, and KPFM measures the changing WF of SLG due to charge exchange at the contact.

In alkaline solution under electrochemical control

Further KPFM experiments were performed on these Cu-decorated samples using the micro-reactor shown in Figure 2a filled with an aqueous 10^{-4} M NaOH solution. The initial V_{WE} (vs V_{CE}) was set to 0 V, then decreased to -1 V in discrete potential steps, holding several minutes for measurement at each setting, followed by increasing to +1 V, and then back down to -0.8 V. KPFM images were acquired under constant-potential conditions (the full set of KPFM images is shown in Figure S5). Representative topography and CPD images at +0.4 V and -0.4 V are shown in Figures 6a and 6b, respectively. Here, two different phenomena occur in concert: 1) doping of SLG due to the applied potential, and 2) change of oxidation state of Cu, which changes the contact doping of SLG.

It is not straightforward to disentangle these two phenomena without reference experiments on bare SLG. Our previous study provides such a reference [18], showing that the behavior can be rationalized by a simple electronic doping (electrochemical gating) model: SLG is doped by electrons at relatively positive potentials and by holes at relatively negative potentials, which is expressed in the WF of suspended SLG. This is called chemical capacitance because it is related to the chemical potential of SLG's electrons, and it is in parallel to the geometrical capacitance of the EDL. Some small deviations from this electronic model appear at higher positive and negative voltages where the oxygen evolution reaction (OER) and hydrogen evolution reaction

(HER) take place, which electrochemically dopes graphene in a manner that counteracts the electronic doping. Importantly, graphene is functionalized with oxygen at high anodic potentials close to 1 V. Another point of reference is the CV curves in Figure 2b, which show that oxidation and reduction of Cu take place below 0 V (vs V_{CE}). The two measurements are different; KPFM measurements capture the steady-state conditions that are established a few minutes after the potential is applied, whereas the electrode-electrolyte interface is not at steady-state during the CV measurements. Moreover, CV measurements require current flow through the solution and through the SLG/Au electrode, whereas KPFM measurements are just a static measure of the state of the system.

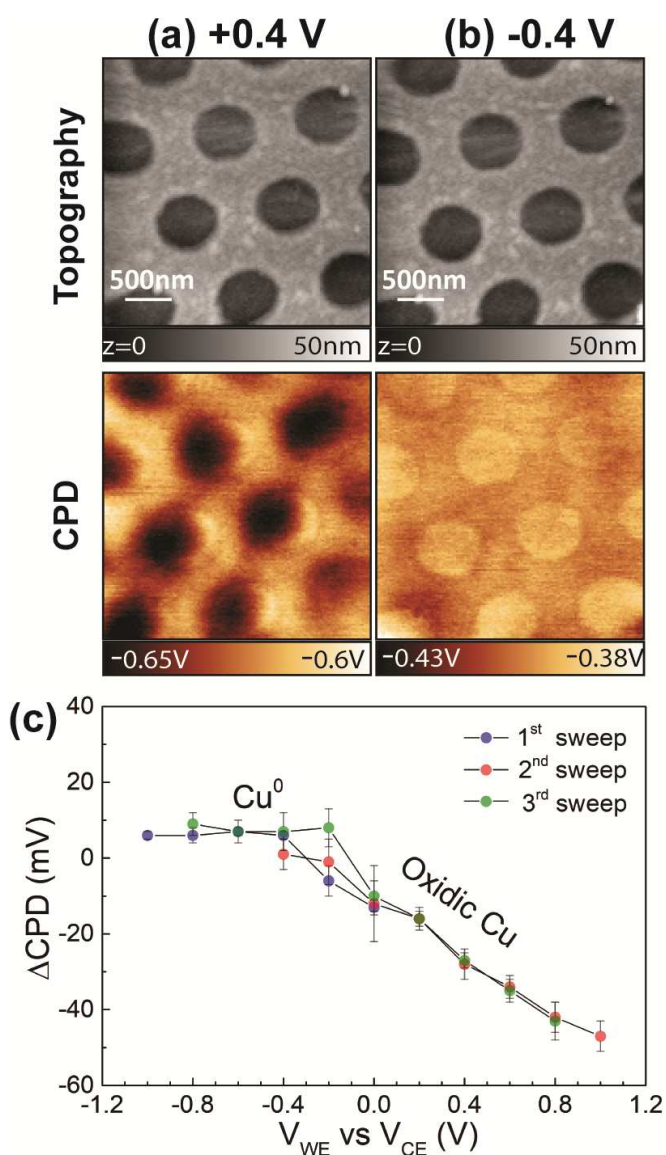


Figure 6. *In-situ* KPFM images under electrochemical reaction conditions: Topography (upper) and CPD (lower) images at (a) +0.4 V (vs V_{CE}) and (b) -0.4 V (vs V_{CE}) acquired during the 3rd sweep. The contrast inversion in CPD images occurs with no evident change in topography. (c) Variations in ΔCPD as a function of the working electrode potential measured using KPFM. Error bars are calculated using Student's t-distribution with a sample size of 7 to 9, i.e., number of circular regions inside the imaged frame. 1st and 3rd "sweeps" are measurements at constant-

potentials with decreasing V_{WE} vs V_{CE} between subsequent conditions. 2nd "sweep" is with increasing V_{WE} vs V_{CE} between subsequent conditions.

Figure 6c summarizes the data of Figure S5 by plotting ΔCPD as a function of cell potential ($V_{WE}-V_{CE}$). The ΔWF of SLG can have contributions from both the charge-carrier doping from the applied potential, and contact doping from Cu NPs that change between metallic and oxidized forms as the potential changes. For bare SLG, ΔCPD shows a quasi-linear trend between -1 V and 1 V at 10^{-4} M NaOH, as doping from the applied potential is the dominant mechanism [18]. For the CuNP-decorated sample, a similar quasi-linear behavior is observed only above ~ -0.3 V (vs V_{CE} , Figure 6c). Below this potential, there is an inflection point and the slope of the trend-line becomes much smaller. A uniform metal with a sufficient thickness has a high density of electronic states and does not undergo band-filling / band-emptying with applied potential; thus, a constant WF should be expected for a perfect metal. Therefore, the electrolyte potential is completely dropped across the geometrical capacitance formed by the EDL. This indicates that below ~ -0.3 V (vs V_{CE}), ΔCPD is simply a measure of the WF difference between SLG in contact with a metallic Cu NP cluster and SLG supported on an Au thin film, independent of the applied potential.

Above ~ -0.3 eV (vs V_{CE}), ΔCPD scales with applied potential almost linearly. For bare SLG, such a behavior can be explained by the bias-dependent electronic doping of graphene [18]. The presence of oxidized NPs does not change this trend due to their semiconducting nature. Electrical contact between the Cu NP clusters and SLG, however, is not lost, as the presence of Cu NP clusters still offsets the SLG WF a few tens of meV due to charge-transfer at the contact. Given the correspondence between adhesion and electronic interaction, we suggest that the NPs

that undergo a complete loss of electrical contact with SLG are those that are also physically detached, and hence contribute to the observed material loss. Remarkably, the effect of material loss on the SLG WF is negligibly small, as the first and third sweeps show similar behavior (Figure 6c). This in turn suggests that the remaining Cu NPs (Figure 4a) are sufficient to screen the electrolyte potential when they are metallic at cathodic potentials, i.e., SLG does not undergo band-filling / band-emptying. We note that the analysis in Figure 6c is from the central $\varnothing 200$ nm region, where the remaining Cu NPs are situated. We also note that the difference between Cu_2O and CuO cannot be distinguished through our measurements here, as a potentially small difference in their hole doping to SLG is overshadowed by the electrochemical gating of graphene.

4. CONCLUSIONS

We present a novel approach for probing NPs under constant-potential electrochemical reaction conditions with KPFM, facilitated by employing a specially designed graphene-capped electrochemical micro-reactor. Our micro-reactor can also be used to conduct conventional electrochemistry experiments such as CV, or *ex-situ* characterization like SEM and TEM imaging. With this approach, we studied the long-term stability of Cu NPs attached to SLG in air, and the stability of the same NPs under electrochemical reaction conditions in an alkaline medium. Initially the surface, and gradually the bulk of the Cu NPs undergo oxidation in ambient air, which we believe to be related to the well-established galvanic corrosion. This, however, is not detrimental as there is no material loss.

We chose a well-known reaction, oxidation and reduction of Cu nanoparticles in an aqueous alkaline solution, as our model electrochemical study. Changes in the oxidation state of Cu are

reflected in the CPD images. Under oxidizing conditions, the CPD trend (as a function of bias) shows a similar behavior to that of bare SLG, which is due to incomplete screening of the electrolyte potential. Under reducing conditions, the CPD is only marginally sensitive to the electrolyte potential, due to screening by the metallic NPs. An important outcome is the detachment of the NPs induced by water intercalation at the weakly interacting CuO-SLG interface, which is enabled by hydrophilicity of SLG at positive potentials. However, we do not observe this adherence problem during faster experiments such as electrochemical cycling, or at negative potentials. Since CO₂ reduction is performed at cathodic conditions where Cu is metallic, and electrochemical cleaning cycles can be rapidly performed, we expect this approach can be extended to the study of Cu as a CO₂ reduction electrocatalyst.

This study thus shows that the graphene-capping approach can be applied for characterizing transition metal / transition metal oxides under electrochemical control, and serves as a benchmark for further studies on more complex reactions where transition metals are used as electrocatalysts.

Declaration of Competing Interest

The authors declare that they have no known competing financial interests or personal relationships that could have appeared to influence the work reported in this paper

Acknowledgements

We are thankful to Dr. Ashley R. Head from the Brookhaven National Laboratory for the XPS measurements. We are also thankful to Dr. Jack Swallow and Dr. Leanne Jones from the Oxford

University for experimental assistance in CV measurements with 3 electrodes. This research was supported by the Minerva Foundation with funding from the Federal German Ministry for Education and Research, and the Weizmann – UK Making Connections Programme. BE acknowledges the support from the Zuckerman STEM Leadership Faculty Fellowship. SK acknowledges the Dean of Faculty of Chemistry Fellowship of the Weizmann Institute of Science. MAA acknowledges the Weizmann Institute “la Caixa” Foundation postdoctoral fellowship. This research used resources of the Center for Functional Nanomaterials (CFN), which is a U.S. Department of Energy Office of Science User Facility, at Brookhaven National Laboratory under Contract No. DE-SC0012704

References

- [1] V. R. Stamenkovic; D. Strmcnik; P. P. Lopes; N. M. Markovic, Energy and Fuels from Electrochemical Interfaces, *Nat. Mater.* 16 (2017) 57–69.
- [2] W. J. Kwak; Rosy; D. Sharon; C. Xia; H. Kim; L. R. Johnson; P. G. Bruce; L. F. Nazar; Y. K. Sun; A. A. Frimer; M. Noked; S. A. Freunberger; D. Aurbach, Lithium-Oxygen Batteries and Related Systems: Potential, Status, and Future, *Chem. Rev.* 120 (2020) 6626–6683.
- [3] C. H. Wu; R. S. Weatherup; M. B. Salmeron, Probing Electrode/Electrolyte Interfaces In-situ By X-Ray Spectroscopies: Old Methods, New Tricks, *Phys. Chem. Chem. Phys.* 17 (2015) 30229–30239.
- [4] A. A. Gewirth; H. Siegenthaler. *Nanoscale Probes of the Solid/Liquid Interface*, Springer Science & Business Media, 2013.

- [5] A. K. Yagati; J. Min; J.-W. Choi, Electrochemical Scanning Tunneling Microscopy (ECSTM) – From Theory to Future Applications, in: Aliofkhazraei, M. (ed), Modern Electrochemical Methods in Nano, Surface and Corrosion Science, IntechOpen, 2014.
- [6] N. Nonnenmacher; M. P. O’Boyle; H. K. Wickramasinghe, Kelvin Probe Force Microscopy, *Appl. Phys. Lett.* 58 (1991) 2921–2923.
- [7] L. Collins; S. Jesse; J. I. Kilpatrick; A. Tselev; M. B. Okatan; S. V. Kalinin; B. J. Rodriguez, Kelvin Probe Force Microscopy in Liquid Using Electrochemical Force Microscopy, *Beilstein J. Nanotechnol.* 6 (2015) 201–214.
- [8] L. Collins; S. A. L. Weber; B. J. Rodriguez, Applications of KPFM-Based Approaches for Surface Potential and Electrochemical Measurements in Liquid, in: S. Sadewasser; T. Glatzel (eds.), *Kelvin Probe Force Microscopy*, Springer International Publishing AG, 2018.
- [9] L. Collins; J. I. Kilpatrick; I. V. Vlassioug; A. Tselev; S. A. L. Weber; S. Jesse; S. V. Kalinin; B. J. Rodriguez, Dual Harmonic Kelvin Probe Force Microscopy at the Graphene–Liquid Interface, *Appl. Phys. Lett.* 104 (2014) 133103.
- [10] M. Krueger; S. Berg; D. Stone; E. Strelcov; D. A. Dikin; J. Kim; L. J. Cote; J. Huang; A. Kolmakov, Drop-Casted Self-Assembling Graphene Oxide Membranes for Scanning Electron Microscopy on Wet and Dense Gaseous Samples, *ACS Nano* 5 (2011) 10047–10054.
- [11] J. M. Yuk; J. Park; P. Ercius; K. Kim; D. J. Hellebusch; M. F. Crommie; J. Y. Lee; A. Zettl; A. P. Alivisatos, High-Resolution EM of Colloidal Nanocrystal Growth Using Graphene Liquid Cells, *Science* 336 (2012) 61–64.

- [12] C. Wang; Q. Qiao; T. Shokuhfar; R. F. Klie, High-Resolution Electron Microscopy and Spectroscopy of Ferritin in Biocompatible Graphene Liquid Cells and Graphene Sandwiches, *Adv. Mater.* 26 (2014) 3410–3414.
- [13] J. Park; H. Elmlund; P. Ercius; J. M. Yuk; D. T. Limmer; Q. Chen; K. Kim; S. H. Han; D. A. Weitz; A. Zettl; A. P. Alivisatos, 3D Structure of Individual Nanocrystals in Solution by Electron Microscopy, *Science* 349 (2015) 290–295.
- [14] J. Park; H. Park; P. Ercius; A. F. Pegoraro; C. Xu; J. W. Kim; S. H. Han; D. A. Weitz, Direct Observation of Wet Biological Samples by Graphene Liquid Cell Transmission Electron Microscopy, *Nano Lett.* 15 (2015) 4737–4744.
- [15] A. Kolmakov; D. A. Dikin; L. J. Cote; J. Huang; M. K. Abyaneh; M. Amati; L. Gregoratti; S. Günther; M. Kiskinova, Graphene Oxide Windows for In-situ Environmental Cell Photoelectron Spectroscopy, *Nat. Nanotechn.* 6 (2011) 651–657.
- [16] J. J. Velasco-Vélez; V. Pfeifer; M. Hävecker; R. S. Weatherup; R. Arrigo; C.-H. Chuang; E. Stotz; G. Weinberg; M. Salmeron; R. Schlögl; A. Knop-Gericke, Photoelectron Spectroscopy at the Graphene–Liquid Interface Reveals the Electronic Structure of an Electrodeposited Cobalt/Graphene Electrocatalyst, *Angew. Chem. Int. Ed.* 54 (2015) 14554–14558.
- [17] R. S. Weatherup; B. Eren; Y. Hao; H. Bluhm; M. B. Salmeron, Graphene Membranes for Atmospheric Pressure Photoelectron Spectroscopy, *J. Phys. Chem. Lett.* 7 (2016) 1622–1627.
- [18] S. Khatun; S. R. Cohen; S. Shor Peled; I. Rosenhek-Goldian; R. S. Weatherup; B. Eren, Observing Electrochemical Reactions on Suspended Graphene: An Operando Kelvin Probe Force Microscopy Approach, *Adv. Mater. Interfaces* 8 (2021) 2100662.

- [19] Y. Hori; A. Murata; R. Takahashi, Formation of Hydrocarbons in the Electrochemical Reduction of Carbon Dioxide at a Copper Electrode on Aqueous Solution, *Faraday Trans. 1* (1989) 2309–2326.
- [20] R. Reske; H. Mistry; F. Behafarid; B. Roldan Cuenya; P. Peter Strasser, Particle Size Effects in the Catalytic Electroreduction of CO₂ on Cu Nanoparticles, *J. Am. Chem. Soc.* 136 (2014) 6978–6986.
- [21] D. C. B. Alves; R. Silva; D. Voiry; T. Asefa; M. Chhowalla, Copper Nanoparticles Stabilized by Reduced Graphene Oxide for CO₂ Reduction Reaction, *Mater. Renew. Sustain. Energy* 4 (2015) 2.
- [22] K. J. Puring; O. Evers; M. Prokein; D. Siegmund; F. Scholten; N. Mölders; M. Renner; B. Roldan Cuenya; M. Petermann; E. Weidner; U.-P. Apfel, Assessing the Influence of Supercritical Carbon Dioxide on the Electrochemical Reduction to Formic Acid Using Carbon-Supported Copper Catalysts, *ACS Catal.* 10 (2020) 12783–12789.
- [23] S. Delgado; M.d.C. Arévalo; E. Pastor; G. García, Electrochemical Reduction of Carbon Dioxide on Graphene-Based Catalysts, *Molecules* 26 (2021) 572.
- [24] R. Blume; P. R. Kidambi; B. C. Bayer; R. S. Weatherup; Z.-J. Wang; G. Weinberg; M.-G Willinger; M. Greiner; S. Hofmann; A. Knop-Gericke; R. Schlögl, The Influence of Intercalated Oxygen on the Properties of Graphene on Polycrystalline Cu under Various Environmental Conditions, *Phys. Chem. Chem. Phys.* 16 (2014) 25989–26003.
- [25] J. Azpeitia; I. Palacio; J. I. Martínez; I. Muñoz-Ochando; K. Lauwaet; F. J. Mompean; G. J. Ellis; M. García-Hernández; J. A. Martín-Gago; C. Munuera; M. F. López, Oxygen Intercalation in PVD Graphene Grown on Copper Substrates: A Decoupling Approach, *Appl. Surf. Sci.* 529 (2020) 147100.

- [26] K. S. Raman; P. C. Banerjee; D. E. Lobo; H. Gullapalli; M. Sumandasa; A. Kumar; L. Choudhary; R. Tkacz; P. M. Ajayan; M. Majumder, Protecting Copper from Electrochemical Degradation by Graphene Coating, *Carbon* 50 (2012) 4040–4045.
- [27] A. Yuan; R. Ran Guan; B. Luo, Oxidative Originators of Graphene Barrier Coating Grown on Surfaces, *ChemNanoMat* 6 (2020) 1285–1297.
- [28] I. Wlasny; P. Dabrowski; M. Rogala; P. J. Kowalczyk; I. Pasternak; W. Strupinski; J. M. Baranowski; Z. Klusek, Role of Graphene Defects in Corrosion of Graphene-coated Cu(111) Surface, *Appl. Phys. Lett.* 102 (2013) 111601.
- [29] M. Schriver; W. Regan; W. J. Gannett; A. M. Zaniwski; M. F. Crommie; A. Zettl, Graphene as a Long-Term Metal Oxidation Barrier: Worse than Nothing, *ACS Nano* 7 (2013) 5763–5768.
- [30] P. Braeuninger-Weimer; O. J. Burton; P. Zeller; M. Amati; L. Gregoratti; R. S. Weatherup; S. Hofmann, Crystal Orientation Dependent Oxidation Modes at the Buried Graphene–Cu Interface, *Chem. Mater.* 32 (2020) 7766–7776.
- [31] J. Ambrose; R. G. Barradas; D. W. Shoesmith, Investigations of Copper in Aqueous Alkaline Solutions by Cyclic Voltammetry, *J. Electroanal. Chem. Interfacial Electrochem.* 47 (1973) 47–64.
- [32] W. Z. Teo; A. Ambrosi; M. Pumera, Direct Electrochemistry of Copper Oxide Nanoparticles in Alkaline Media, *Electrochem. Commun.* 28 (2013) 51–53.
- [33] S. L. Marchiano; C. I. Elsner; A. J. Arvia, The Anodic Formation and Cathodic Reduction of Cuprous Oxide Films on Copper in Sodium Hydroxide Solutions, *J. Appl. Electrochem.* 10 (1980) 365–377.

- [34] H.-H. Strehblow; V. Maurice; P. Marcus, Initial and Later Stages of Anodic Oxide Formation on Cu, Chemical Aspects, Structure and Electronic Properties, *Electrochimica Acta* 46 (2001) 3755–3766.
- [35] F. Caballero-Briones; J. M. Artés; I. Díez-Pérez; P. Gorostiza; F. Sanz, Direct Observation of the Valence Band Edge by In-situ ECSTM-ECTS in p-Type Cu₂O Layers Prepared by Copper Anodization, *J. Phys. Chem. C* 113 (2009) 1028–1036.
- [36] B. Eren; Ch. Heine; H. Bluhm; G. A. Somorjai; M. Salmeron, Catalyst Chemical State during CO Oxidation Reaction on Cu(111) Studied with Ambient-Pressure X-ray Photoelectron Spectroscopy and Near Edge X-ray Adsorption Fine Structure Spectroscopy, *J. Am. Chem. Soc.* 137 (2015) 11186–11190.
- [37] P. Jiang; D. Prendergast; F. Borondics; S. Porsgaard; L. Giovanetti; E. Pach; J. Newberg; H. Bluhm; F. Besenbacher; M. Salmeron, Experimental and Theoretical Investigation of the Electronic Structure of Cu₂O and CuO Thin Films on Cu(110) Using X-Ray Photoelectron and Absorption Spectroscopy, *J. Chem. Phys.* 138 (2013) 024704.
- [38] S. Y. Lee; N. Mettlach; N. Nguyen; Y. M. Sun; J. M. White, Copper Oxide Reduction through Vacuum Annealing, *Appl. Surf. Sci.* 206 (2003) 102–109.
- [39] P. Keil; D. Lutzenkirche-Hecht; R. Frahiri, Investigation of Room Temperature Oxidation of Cu in Air by Yoneda-XAFS, *AIP Conf. Proc.* 882 (2006) 490–492.
- [40] Y. Zhang; O. Pluchery; L. Caillard; A.-F. Lamic-Humblot; S. Casale; Y. J. Chabal; M. Salmeron, Sensing the Charge State of Single Gold Nanoparticles via Work Function Measurements, *Nano Lett.* 15 (2015) 51–55.

- [41] B. Beverskog; I. Puigdomenech, Revised Pourbaix Diagrams for Copper at 25 to 300°C, *J. Electrochem. Soc.* 144 (1997) 3476–3483.
- [42] A. I. Aria; P. R. Kidambi; R. S. Weatherup; L. Xiao; J. A. Williams; S. Hofmann, Time Evolution of the Wettability of Supported Graphene under Ambient Air Exposure, *J. Phys. Chem. C* 120 (2016) 2215–2224.
- [43] Z. Gu; H. Shen; L. Shang; X. Lv; L. Qian; G. Zheng, Nanostructured Copper-Based Electrocatalysts for CO₂ Reduction, *Small Methods* 2 (2018) 1800121.
- [44] R. Chen; C. Yang; W. Cai; H.-Y. Wang; J. Miao; L. Zhang; S. Chen; B. Liu, Use of Platinum as the Counter Electrode to Study the Activity of Nonprecious Metal Catalysts for the Hydrogen Evolution Reaction, *ACS Energy Lett.* 2 (2017) 1070–1075.
- [45] E. L. Clark; J. Resasco; A. Landers; J. Lin; L.-T. Chung; A. Walton; C. Hahn; T. F. Jaramillo; A. T. Bell. Standards and Protocols for Data Acquisition and Reporting for Studies of the Electrochemical Reduction of Carbon Dioxide, *ACS Catal.* 8 (2018) 6560–6570.
- [46] G. Giovannetti; P. A. Khomyakov; G. Brocks; V. M. Karpan; J. van den Brink; P. J. Kelly, Doping Graphene with Metal Contacts, *Phys. Rev. Lett.* 101 (2008) 026803.
- [47] M. M. Giangregorio; W. Jiao; G. V. Bianco; P. Capezzuto; A. S. Brown; G. Bruno; M. Losurdo, Insights into the Effects of Metal Nanostructuring and Oxidation on the Work Function and Charge Transfer of Metal/Graphene Hybrids, *Nanoscale* 7 (2015) 12868–12877.
- [48] S. Gottardi; K. Müller; L. Bignardi; J. C. Moreno-López; T. A. Pham; O. Ivashenko; M. Yablonskikh; A. Barinov; J. Björk; P. Rudolf; M. Stöhr, Comparing Graphene Growth on Cu(111) versus Oxidized Cu(111), *Nano Lett.* 15 (2015) 917–922.

- [49] Y. Zhang; O. Pluchery; L. Caillard; A.-F. Lamic-Humblot; S. Casale; Y. J. Chabal; M. Salmeron, Sensing the Charge State of Single Gold Nanoparticles via Work Function Measurements, *Nano Lett.* 15 (2015) 51–55.
- [50] S. Brittman; Y. Yoo; N. P. Dasgupta; S. Kim; B. Kim; P. Yang, Epitaxially Aligned Cuprous Oxide Nanowires for All-Oxide, Single-Wire Solar Cells, *Nano Lett.* 14 (2014) 4665–4670.
- [51] H. Raebiger; S. Lany; A. Zunger, Origins of the p-type Nature and Cation Deficiency in Cu_2O and Related Materials, *Phys. Rev. B* 76 (2007) 045209.
- [52] D. Wu; Q. Zhang, LSDA+U Study of Cupric Oxide: Electronic Structure and Native Point Defects, *Phys. Rev. B* 73 (2006) 235206–235212.
- [53] S. Hudlet; M. Saintjean; B. Roulet; J. Berger; C. Guthmann, Electrostatic Forces between Metallic Tip and Semiconductor Surfaces, *J. Appl. Phys.* 77 (1995) 3308.
- [54] W. Melitz; J. Shen; A. Kummel; S. Lee, Kelvin Probe Force Microscopy and Its Application, *Surf. Sci. Rep.* 66 (2011) 1–27.